

Turbulence in the Orion Nebula

S.-N. X. Medina¹, S. J. Arthur^{2*}, W. J. Henney²

¹Max Planck Institut für Radioastronomie, Bonn, Germany.

²Instituto de Radioastronomía y Astrofísica, Universidad Nacional Autónoma de México, Campus Morelia, 58090 Morelia, Michoacán, México.

ABSTRACT

Non-thermal linewidths in compact HII regions such as the Orion Nebula can plausibly be explained in terms of transonic turbulence. However, the driving mechanism of the turbulence remains uncertain. We analyze the observational data from the atlas of optical emission-line velocities in the Orion Nebula constructed by García-Díaz, Henney et al (2008, RMxAA 44, 181) using second-order structure functions of the velocity centroid maps and velocity channel analysis of the individual long-slit spectra. The results of this statistical analysis allow us to investigate the driving scales of the turbulence in the ionized gas. We compare our findings with the results obtained from a similar analysis of a numerical simulation of an HII region. We find that...

*Remove Arthur
from abstract*

Key words: hydrodynamics — HII regions — ISM: kinematics and dynamics — turbulence

1 INTRODUCTION

NECESITA TRABAJO:

The line broadening in excess of thermal broadening seen in optical spectroscopic studies of H II regions has been attributed to turbulence in the photoionized gas. There are many examples in the literature of attempts to identify the presence and characterize this turbulence, for example Münch (1958), Roy & Joncas (1985), O'Dell & Castañeda (1987), Miville-Deschénes, Joncas, & Durand (1995), Medina-Tanco et al. (1997), Lagrois & Joncas (2011) and references cited by these papers. In these studies, the variation of the point-to-point radial velocities with scale was investigated using structure functions following von Hoerner (1951).

In order to construct the structure functions for the velocity fields, observations at many points in an H II region are needed. This can be achieved either by multiple longslit spectroscopic observations at many positions across a nebula (O'Dell, Townsley, & Castañeda 1987; Castañeda & O'Dell 1987; Wen & O'Dell 1993), or by Fabry-Perot interferometry (Roy & Joncas 1985; Miville-Deschénes, Joncas, & Durand 1995; Lagrois et al. 2011). Longslit observations with high velocity resolution have enabled several velocity components to be identified for emission lines of metal ions for which the thermal widths are small, e.g., [O III] $\lambda 5007$. These observations have been used to determine the radial velocities of the principal components of the emitting gas at hundreds of positions within the nebula. Fabry-Perot observations produce datasets of thousands of radial velocities, but without

the velocity resolution to distinguish between different velocity components. Obviously, in order to obtain a structure function over a wide range of scales, very high quality data with an ample spatial coverage are required. In the case of longslit spectra, this is a non-trivial task, not least the calibrating of the positions of the slits (García-Díaz & Henney 2007; García-Díaz et al. 2008).

In a previous paper we investigated the scale dependence of fluctuations inside a realistic model of an evolving turbulent HII region and to what extent these may be studied observationally. We found that the multiple scales of energy injection from champagne flows and the photoionization of clumps and filaments lead to a flatter spectrum of fluctuations than would be expected from top-down turbulence driven at the largest scales. The traditional structure function approach to the observational study of velocity fluctuations was shown to be incapable of reliably determining the velocity power spectrum of our simulation. We found that a more promising approach is the Velocity Channel Analysis technique of Lazarian & Pogosyan (2000), which, despite being intrinsically limited by thermal broadening, can successfully recover the logarithmic slope of the velocity power spectrum to a precision of ± 0.1 from high resolution optical emission line spectroscopy.

2 METHODS

We calculate second-order structure functions of the velocity centroid maps and also perform a velocity channel analysis on the individual slits.

For the structure functions we use the 2D smoothed

* E-mail: j.arthur@crya.unam.mx

So for [OIII] we have observed $\sigma = 10 \text{ km/s} \Rightarrow \sigma_{\text{tot}}^2 = 100 \text{ km}^2 \text{s}^{-2} = \sigma_{\text{los}}^2 + \sigma_{\text{turb}}^2 + \sigma_{\text{ins}}^2$

2 S.-N. X. Medina et al.

These points should probably be masked out too

$$\sigma_{\text{ins}}^2, \sigma_{\text{turb}}^2 \text{ both } < 10 \text{ km}^2 \text{s}^{-2}$$

$$\text{for [OIII]} \Rightarrow \sigma_{\text{los}}^2 \gg 80 \text{ km}^2 \text{s}^{-2}$$

$$\Rightarrow \sigma_{\text{los}} \approx 9 \text{ km/s}$$

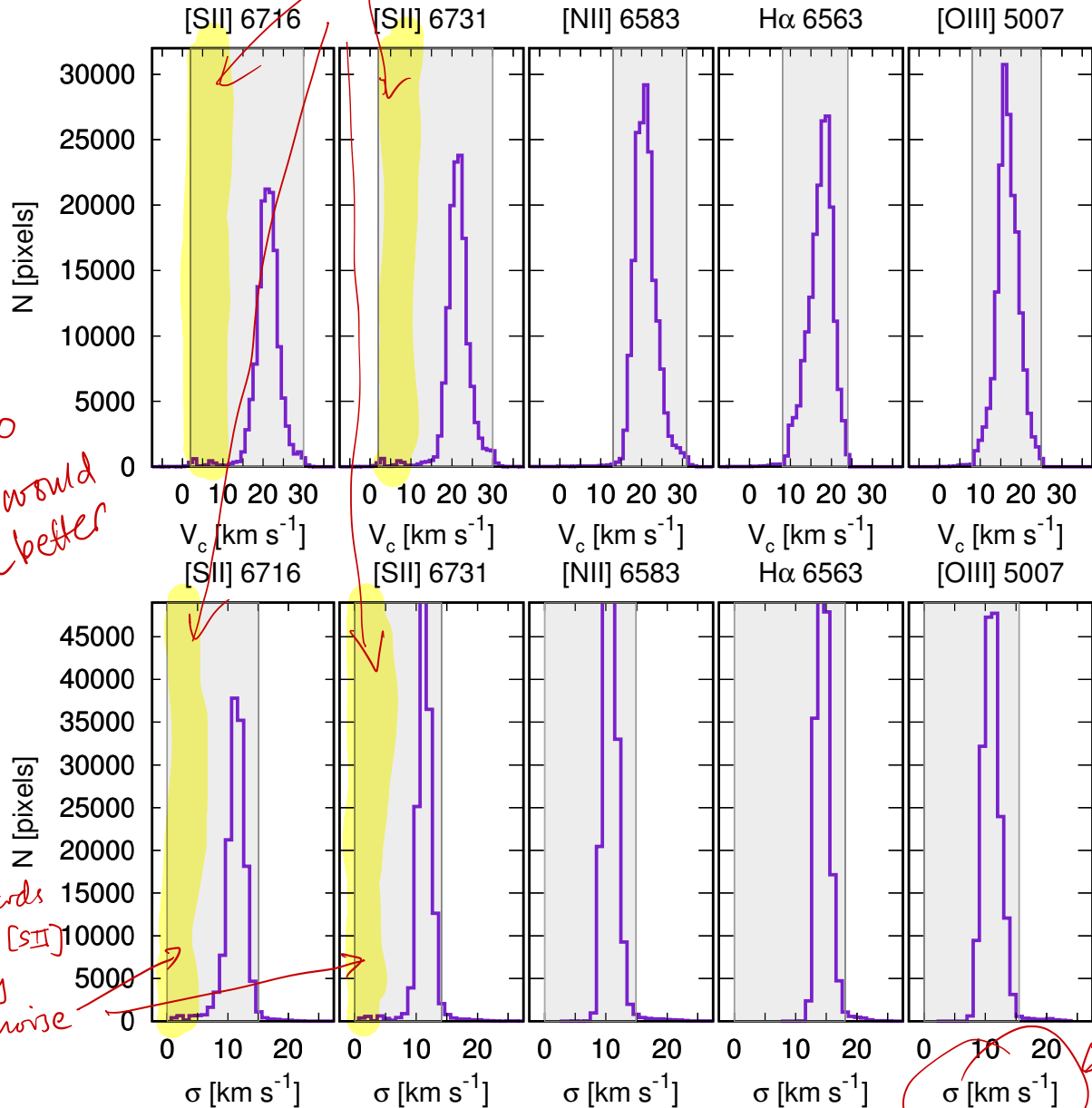


Figure 1. Probability density functions (pdf) of the [SII] $\lambda 6716 \text{ \AA}$ and [SII] $\lambda 6731 \text{ \AA}$ [NII] $\lambda 6584 \text{ \AA}$, H α and [OIII] $\lambda 5007 \text{ \AA}$, emission line velocity centroids (top panel) and velocity dispersions (bottom panel). The shaded grey areas indicate the selected ranges of the centroid velocities and velocity dispersions used to create masks.

Space : [NII], etc. Use `violinplot2` command ?

combined velocity centroid maps of the H α $\lambda 6583$, [NII] $\lambda 6583$, [OIII] $\lambda 5007$, [SII] $\lambda 6716$ and [SII] $\lambda 6731$ lines from the emission line atlas published by García-Díaz et al. The [OI] and [SIII] maps are too noisy to be of any use.

The first step is to examine the pdf of the velocity centroid map and the corresponding velocity dispersion map. We try to eliminate pixels associated with small-scale high velocity features such as jets and Herbig-Haro objects, as these will affect the structure function but are not associated with the underlying turbulence. Also, pixels having an anomalously large velocity dispersion are suggestive of multiple velocity components contributing to the emission line and these, too are identified and eliminated. In practice, a 2% threshold was uniformly applied to the velocity centroid pdf binned at 1 km s^{-1} resolution. The same threshold was

also applied to one side of the velocity dispersion pdf binned at 1 km s^{-1} resolution to eliminate the small number of pixels with anomalously high values. Figure 1 shows the initial pdfs of the centroid velocities and the velocity dispersions of the 5 emission lines studied in this paper together with the ranges of values used to create masks.

Figures 2 and 3 show the 2D interpolated velocity centroid maps together with the masks constructed from pixels with extreme values of the centroid velocity or velocity dispersion identified through consideration of the pdfs. It can be seen that these pixels correspond to high velocity features, such as HH 201, 202, 203, 204, and 529, and also to numerical artefacts introduced during the original construction of the maps from the individual slits.

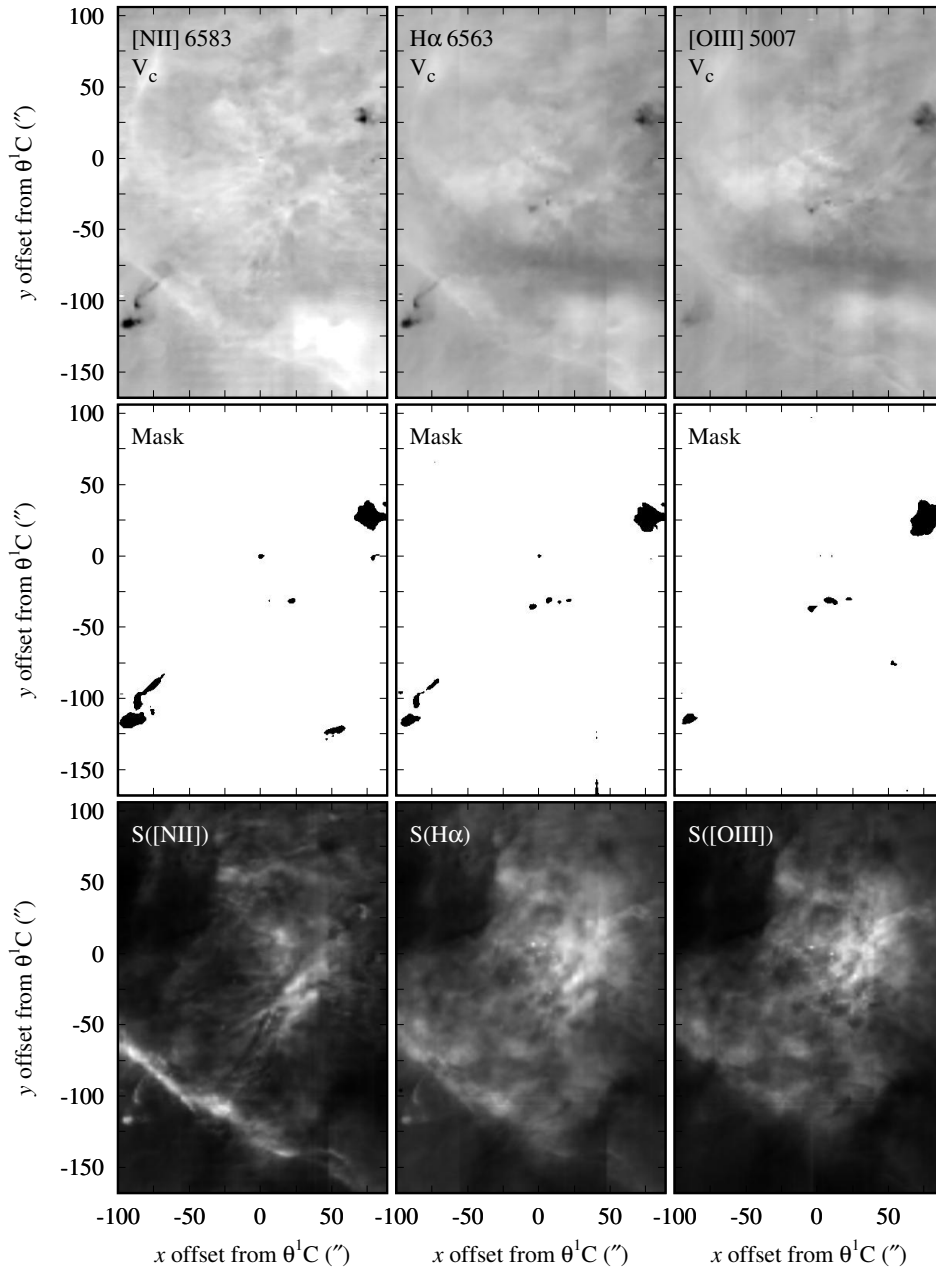


Figure 2. Two-dimensional interpolated maps of velocity centroids of the (left to right) [NII] $\lambda 6584 \text{ \AA}$, H α and [OIII] $\lambda 5007 \text{ \AA}$ emission lines. The upper panels show the initial 2D interpolated velocity centroid maps with a linear greyscale between -40 and 70 km s^{-1} . The centre panels show the masks obtained by eliminating pixels with extreme values of the centroid velocity or velocity dispersion. The lower panels show the integrated intensity (surface brightness) with a linear greyscale.

2.1 Velocity Channel Analysis

The velocity channel analysis consists of taking the 1D spatial power spectrum of the spectroscopic PV data from each slit observation. First, the PV data is binned into velocity *channels*, which can be *thin* or *thick*. The relative contribution of velocity fluctuations to fluctuations in the total intensity decreases as the width of the velocity slices increases, because thicker velocity slices average out the contributions of many velocity fluctuations. A velocity slice has width $\delta v = (v_{\max} - v_{\min})/N$, where N is the number of chan-

nels and for the spectra used in this work $v_{\max} = 70 \text{ km s}^{-1}$ and $V_{\min} = -40 \text{ km s}^{-1}$.

The thickest velocity channel ($N = 1$) corresponds to the total emission line surface brightness at each pixel along the slit. The thinnest velocity slices are chosen to have $\delta v = 4 \text{ km s}^{-1}$, to give a good sampling of the spectrograph velocity resolution of $6\text{--}8 \text{ km s}^{-1}$ for the H α , [NII] $\lambda 6583$ and [OIII] $\lambda 5007$ emission lines and 2 km s^{-1} for the [SII] $\lambda 6716$ and [SII] $\lambda 6731$ emission lines. To use thinner velocity slices would be to amplify the noise (see Medina et al. 2014, hereafter Paper I). Accordingly, our thinnest velocity slices have $\delta v = 4 \text{ km s}^{-1}$

*for
or not?*

Might make more sense to use a common mask for the [N^{II}] and both [SII] lines (although might be problematic to put [N^{II}] and [SII] on a common grid.)

Make clearer that each slit is treated separately. Explain due to better spatial resolution along slit, and to potential slit-to-slit calibration errors.

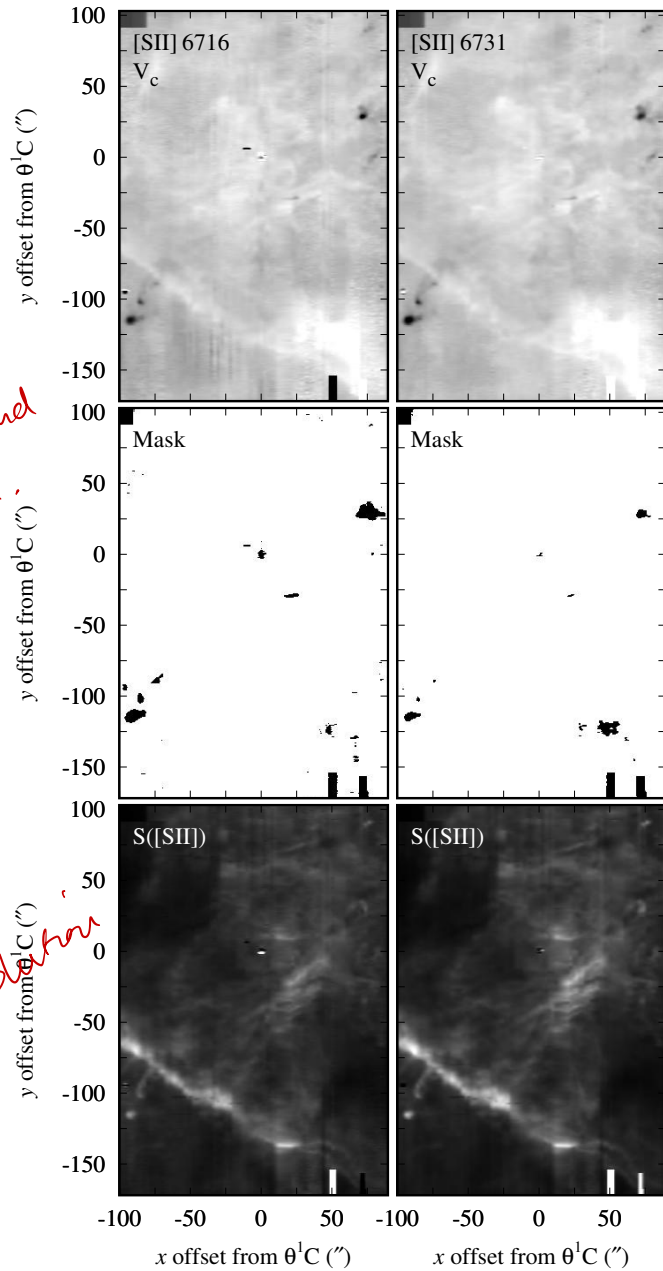


Figure 3. Same as Fig. 2 but for the [SII] $\lambda 6716 \text{ \AA}$ and [SII] $\lambda 6731 \text{ \AA}$ emission lines.

The power spectra for each velocity slice of each 1D spectroscopic observation for a given emission line are summed and normalized by the total power. The power spectra are calculated with a fast fourier transform technique. Since each spectroscopic observation corresponds to a finite slit length, we use a Welch window function to reduce the edge effects in the estimated power spectrum (?).

2.2 Second-order Structure Functions

The second-order structure function of the velocity centroids is (see Paper I)

$$S_2(\mathbf{l}) = \frac{\sum_{\text{pairs}} [V_c(\mathbf{r}) - V_c(\mathbf{r} + \mathbf{l})]^2}{\sigma_{vc}^2 N(\mathbf{l})}. \quad (1)$$

Maybe also give equations for flux-weighted version. That is - bring in Eq (4) from page 8 to here.

In this definition, \mathbf{r} is the two-dimensional position vector in the plane of the sky, while \mathbf{l} is the separation vector. The normalization is by the number of pairs of points at each separation, $N(\mathbf{l})$, and the variance of centroid velocity fluctuations, σ_{vc}^2 , defined by

$$\sigma_{vc}^2 \equiv \frac{\sum_{\text{pixels}} [V_c(\mathbf{r}) - \langle V_c \rangle]^2}{N}. \quad (2)$$

Here, $\langle V_c \rangle$ is the mean centroid velocity

$$\langle V_c \rangle \equiv \frac{\sum_{\text{pixels}} V_c(\mathbf{r})}{N}. \quad (3)$$

The summation in Equation 1 is over all data pairs for each separation, $N(\mathbf{l})$, while the summations in the centroid vari-

Better: "less negative than -3". Also, give name γ to the power-law index, or maybe "shallower than -3" — and say $\gamma \approx -3$ corresponds to $k^3 P(k)$ increasing with k in the graph.

ation and mean (Eqs. 2 and 3) are over the total number of array elements, i.e., valid pixels in the (x, y) -plane.

In order to estimate the effects of large-scale spatial inhomogeneity we additionally evaluate the second-order structure function for 100 distinct, randomly selected rectangular frames within each 2D map. Each frame has two-thirds the x and y dimension of the initial map. The motivation behind this is that the Orion nebula is a very complex, inhomogeneous object with ill-defined boundaries. Taking the full 2D velocity centroid map will inevitably include regions where the turbulence is not homogeneous. The structure functions calculated for the smaller maps give us an idea of the spread of power-law behaviour due to location.

Refer to Fig 4 here.

3 RESULTS

3.1 Velocity Channel Analysis

The 1D, normalised, compensated power spectra for thin (4 km s^{-1}) and thick velocity channels are shown for all emission lines in Figures 5 and 6. The coloured points represent the average power spectrum of 96 distinct slits, in the case of the [NII] $\lambda 6583$, H α , and [OIII] $\lambda 5007$ emission lines, where the slits cover uniformly the region shown in the velocity centroid maps. In the case of the two [SII] emission lines, only the 20 highest resolution slits are used, since the other slits are too affected by noise at high wavenumber (see Fig. 7 for the positions of the 20 slits and García-Díaz et al. 2008 for observational details).

By plotting $k^3 P(k)$ it becomes very apparent that there is a break in the power-law behaviour around wavenumber $k = 0.124 \text{ arcsec}^{-1}$ ($k = 0.144 \text{ arcsec}^{-1}$ for the SII lines). This corresponds to a size scale of $7 - 8 \text{ arcsec}$. For wavenumbers smaller than this break point (i.e., larger lengthscales) the power-law indices of all the power spectra for all the emission lines are all > -3 for the thin velocity channels and also for the thick channels, with the exception of the [SII] emission lines, where the power law index is ~ -3 . In all cases the power laws for the thin channels are less steep than those of the thick channels. For larger wavenumbers than the break point (smaller spatial scales) the power-law indices are all steeper than -3 , indicating that there is very little power at small spatial scales. For $k > 0.3 \text{ arcsec}^{-1}$ (lengthscales $< 3 \text{ arcsec}$) the power spectra are just showing noise. *mention that $k^3 P(k)$ starts rising again*.

The power-law indices of the H α and [OIII] emission line power spectra for the thin slices are steeper than those of the [NII] power spectra. In general, the [OIII] and [NII] power spectra are less noisy than the H α one. The [SII] power spectra are the steepest of all but the power spectrum behaviour of the two different [SII] emission lines is essentially identical.

We estimate confidence bounds on the fitted power-law indices (Table 1) via a bootstrap monte carlo method (resampling with replacement of the set of slits). These spreads are not primarily due to observational uncertainties, which are small for $k < 0.2 \text{ arcsec}^{-1}$, but rather to large-scale inhomogeneity of the *power spectrum*. The power spectra resulting from 10 different slit resamplings are shown in grey in Figures 5 and 6.

The overall shape of the compensated power spectra are

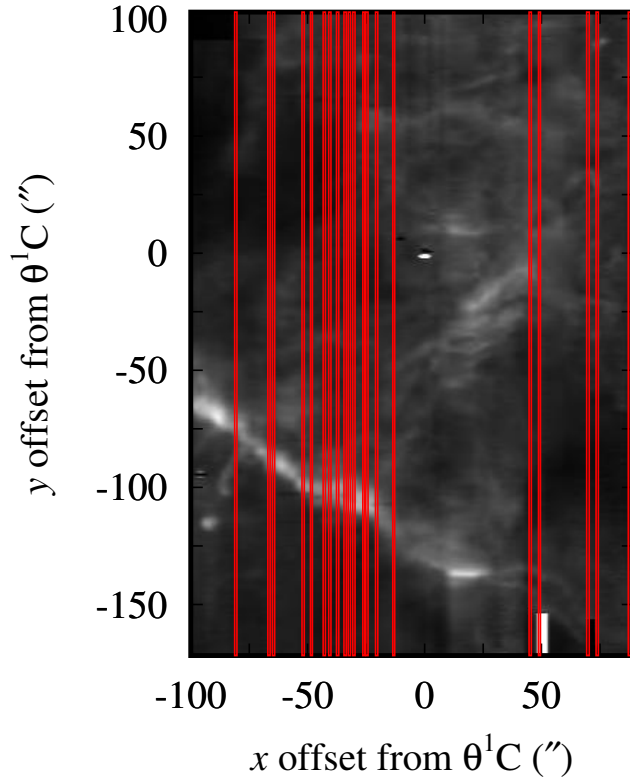


Figure 7. Positions of the 20 high spatial resolution [SII] slits superimposed on the [SII] $\lambda 6716$ surface brightness image.

qualitatively similar for all lines and for both thin and thick slices. In particular, the break in the slope always occurs at the same scale: $7 - 8 \text{ arcsec}$, indicating that it must be a feature of the emissivity fluctuations in the nebula. The power spectrum of the thin slices is generally shallower (less negative) than that of the thick slices, which is indicative of the additional effect of velocity fluctuations (discussed in more depth in § 3.3).

Better start by saying there are four regimes of k , ignoring $k < 0.01 \text{ arcsec}^{-1}$, since that is affected by edges. SEE NEXT PAGE

3.2 Second-order Structure Functions

3.2.1 Shape and Slope of Structure Function for each emission line

We use Equation 1 to calculate the second-order structure functions of the velocity centroid maps for the [NII] $\lambda 6583$, H α , [OIII] $\lambda 5007$, [SII] $\lambda 6716$ and [SII] $\lambda 6731$ emission lines. Figures 8 and 9 (top panels) show the complete structure function of the pdf-selected pixels, together with the structure functions obtained from 100 smaller rectangular boxes within the velocity centroid map (see Fig. 4). The fit to the power-law index of the structure function is performed over the spatial separations indicated by the velocity channel analysis ($8 < l < 22 \text{ arcsec}$ for the [NII], H α and [OIII] emission lines, and $7 < l < 32 \text{ arcsec}$ for [SII] emission lines). The noise, estimated to be equal to the structure function for one pixel separation $S_2(1)$, has been subtracted from the figures. Unlike in the case of the power spectra, the structure functions show no clear break at a scale of $\sim 8 \text{ arcsec}$. The power-law fit to scales $> 8 \text{ arcsec}$ is not too bad a fit to smaller scales also. However, there is a slight negative

Four regimes: I. $k=0.01-0.03$, $\gamma = -1--2$: uncorrelated?
 II. $k=0.03-0.13$, $\gamma = -2--3$: shallow
 III. $k=0.13-0.4$, $\gamma \approx -4$: steep
 IV. $k > 0.4$, $\gamma \approx -1$: noise (uncorrelated)

6 S.-N. X. Medina et al.

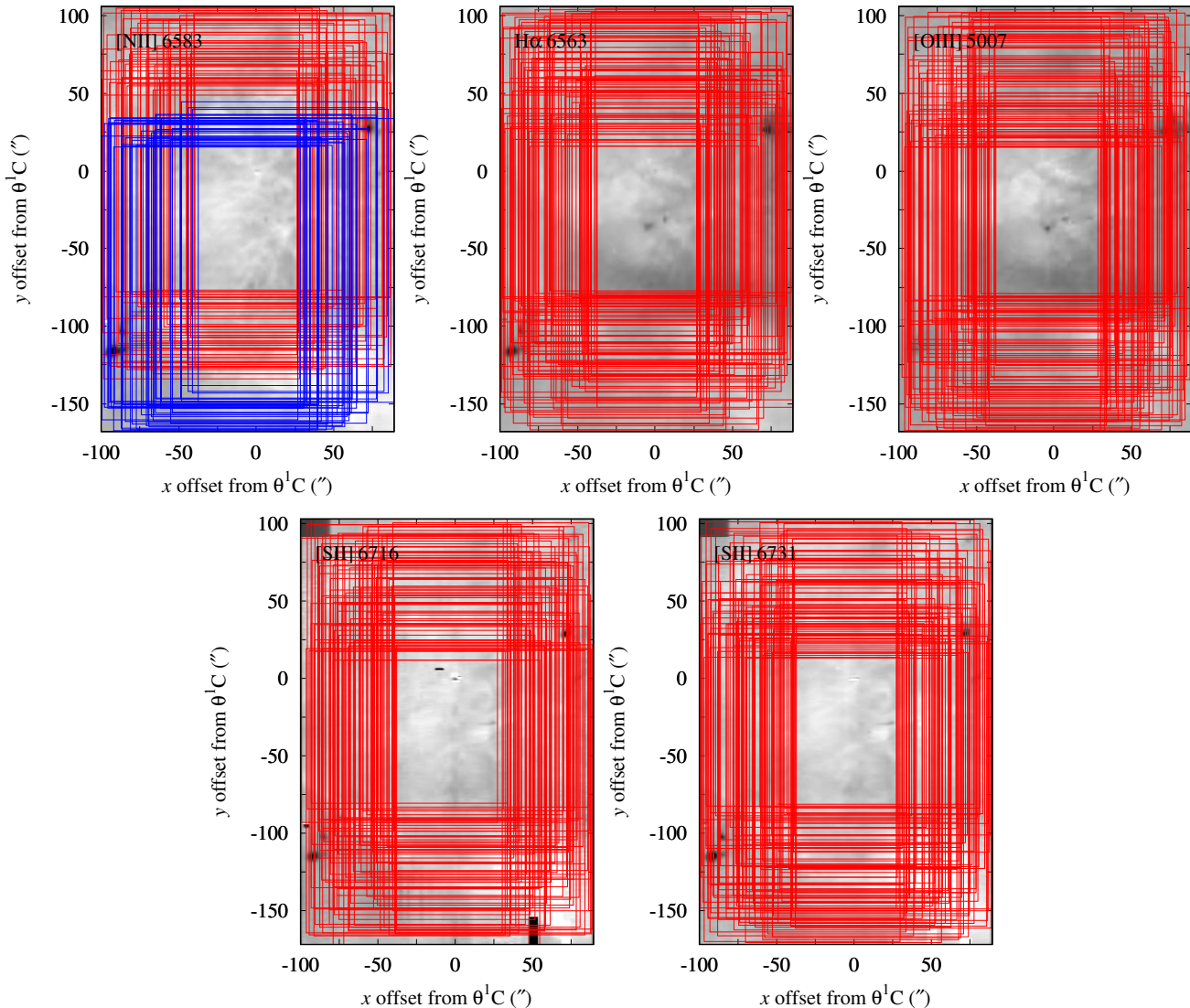


Figure 4. Distribution of randomly selected rectangular frames for the structure function calculations. Top row: [NII], H α and [OIII] frames. The [NII] frames show the spatial separation of the two distinct structure function populations (depicted with red and blue rectangles). Bottom row: frames for the two [SII] emission lines.

Emission Line	k_1	k_2	k_3	Thin γ_{t1}	Thick γ_{T1}	Thin γ_{t2}	Thick γ_{T2}
	$arcsec^{-1}$				$k_1 < k < k_2$		$k_2 < k < k_3$
[SII] $\lambda 6716$	0.031	0.144	0.213	-2.72 ± 0.12	-3.06 ± 0.13	-4.45 ± 0.32	-5.21 ± 0.43
[SII] $\lambda 6731$	0.031	0.144	0.213	-2.69 ± 0.11	-3.03 ± 0.14	-4.69 ± 0.42	-5.16 ± 0.60
[NII] $\lambda 6583$	0.044	0.124	0.274	-2.30 ± 0.08	-2.58 ± 0.09	-4.14 ± 0.11	-4.14 ± 0.13
H α 6563	0.044	0.124	0.256	-2.70 ± 0.12	-2.79 ± 0.15	-4.40 ± 0.12	-4.26 ± 0.16
[OIII] $\lambda 5007$	0.044	0.124	0.311	-2.53 ± 0.08	-2.82 ± 0.10	-4.03 ± 0.11	-3.68 ± 0.25

Table 1. Slopes of power-law fits to power spectra of the velocity channels for the different emission lines.

curvature, giving gradually steeper slopes at smaller scales. The more pronounced steepening below 2 arcsec is due to the spatial resolution and the seeing and inter-slit separation become important. In the figures, we only plot the structure function up to spatial separations $l = 120$ arcsec. Above this value, the structure function falls away steeply.

due to edge effects?

The steepest power-law indices over the fit range are for the H α and [OIII] emission lines. The form of the structure function curves is the same for both emission lines and the value of the power-law index is $m_{2D} \sim 1.2 \pm 0.1$ in both cases. The two [SII] emission lines have very similar structure functions to each other. Their slopes are shallower

The low- k range ($< 0.03 \text{ arcsec}^{-1}$) is also worth discussing.
 Looks close to the same slope as for the noise ($\gamma = -1$?).
 So presumably, it is spatially uncorrelated variations on 30'' scale

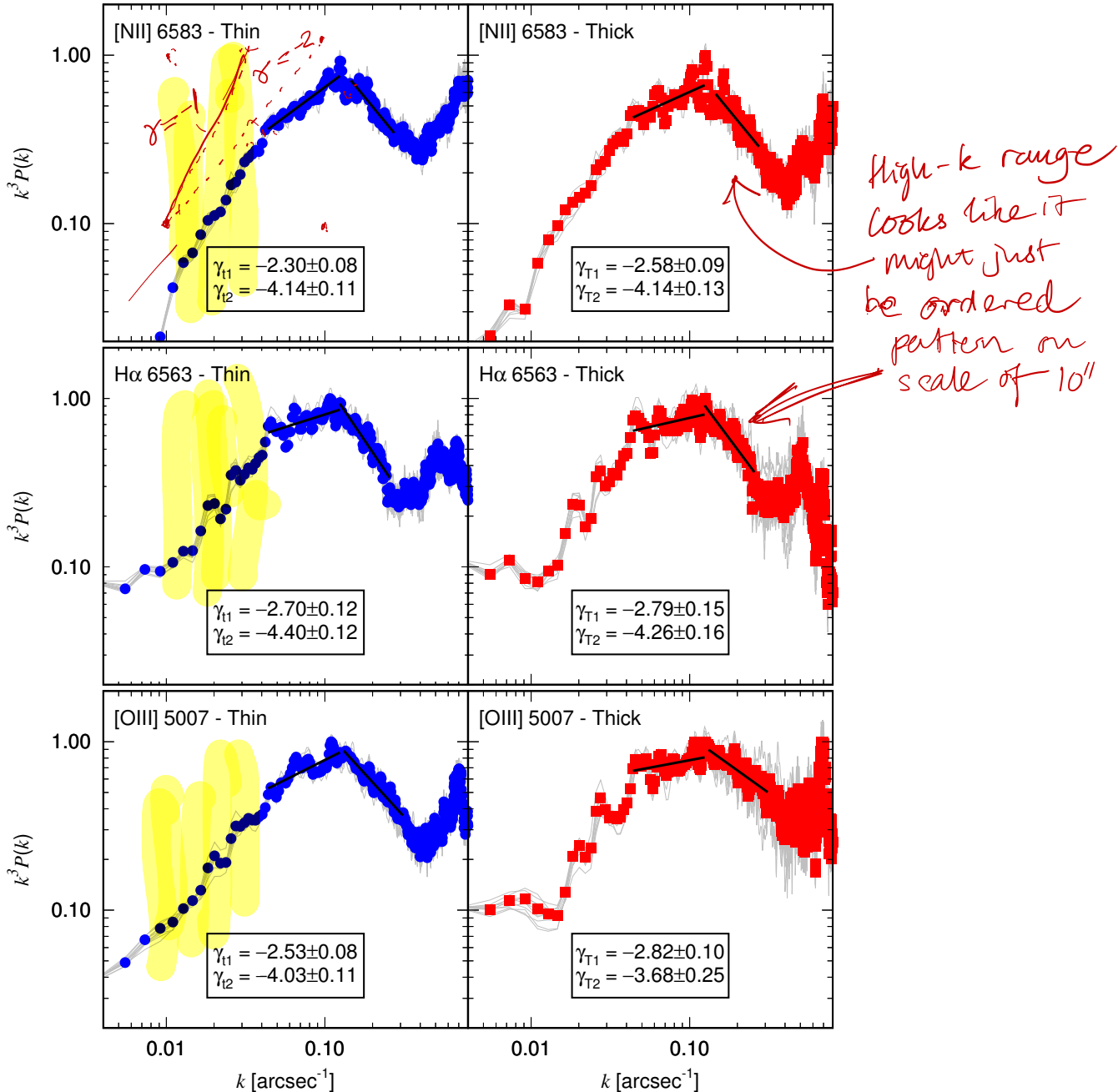


Figure 5. Compensated power spectra of the velocity channels for the [NII], H α and [OIII] emission lines for thick (one slice) and thin (32 slices) velocity slices in the velocity range -40 to 70 km s^{-1} . Also shown are the least-squares fits to the data points for wavenumber ranges corresponding to power-law indices steeper than -3 and power-law indices shallower than -3 .

clearer to say "northern" and "southern"?

than those of the H α and [OIII] structure functions, having $m_{2D} \sim 0.8 \pm 0.1$. There is considerable variation at the smallest scales in the structure function among the different selected boxes. Finally, the structure functions for the [NII] line can be divided into two distinct populations: one set corresponds to boxes selected from the upper part of the velocity centroid map, the other to boxes from the lower half (see Figure 4). One set has a power-law index similar to that of the [SII] lines, while the other is intermediate between the [SII] and H α cases.

native structure functions for the same emission-line velocity centroid maps. The solid red circles show the same pdf-selected structure functions as in the upper panels, while the solid blue triangles show the structure functions obtained when all the pixels are used. There is little difference between the two structure functions for the [NII], H α and [OIII] emission lines but the [SII] structure functions show considerable differences. This is because more pixels are eliminated from the velocity centroid maps on the basis of the pdf analysis for the [SII] lines: some of these pixels correspond to high-velocity features, such as HH objects,

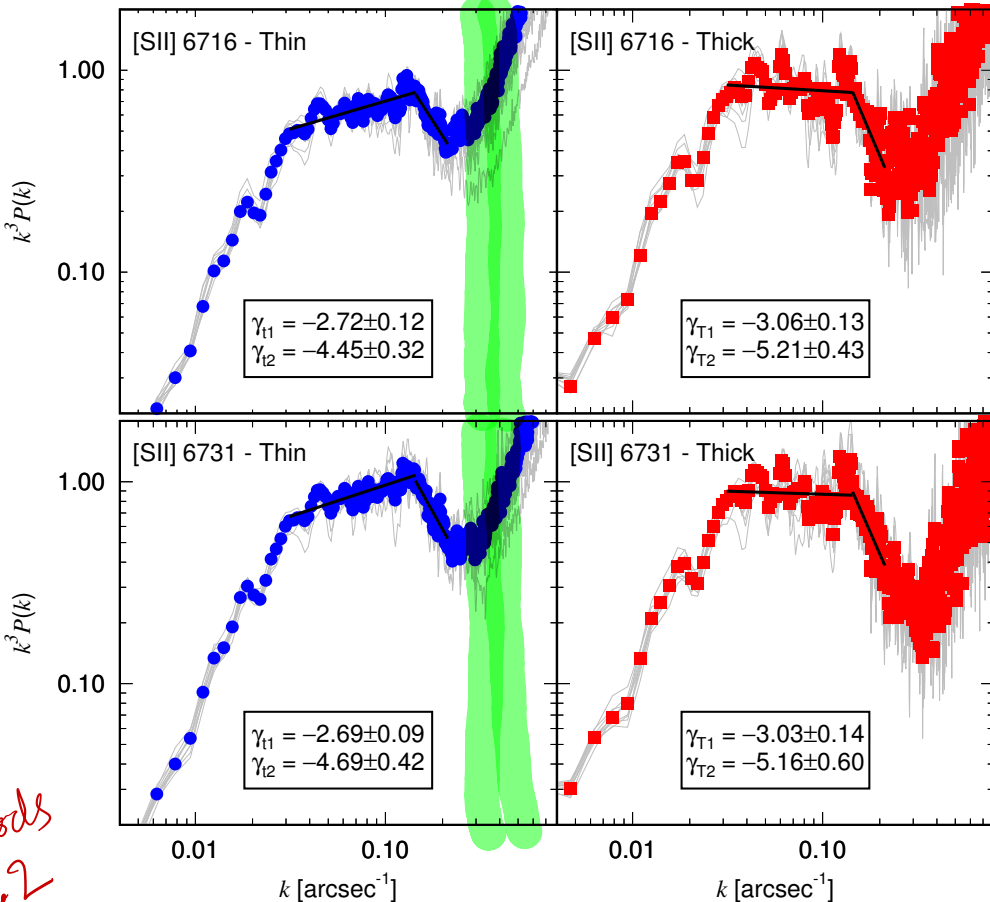


Figure 6. Same as Fig. 5 but for the [SII] 6716 and [SII] 6731 emission lines.

while others correspond to numerical noise. Evidently, these pixels influence the structure function.

Also in the lower panels of Figures 8 and 9, we plot the intensity weighted structure functions of the corresponding cases. That is, instead of using the structure function $S_2(l)$ as defined by Equation 1, we use the following definition

$$S_2(l) = \frac{\sum_{\text{pairs}} [V_c(\mathbf{r}) - V_c(\mathbf{r} + \mathbf{l})]^2 I(\mathbf{r}) I(\mathbf{r} + \mathbf{l})}{\sigma_{vc}^2 W(l)}, \quad (4)$$

where $W(l) = \sum_{\text{pairs}} I(\mathbf{r}) I(\mathbf{r} + \mathbf{l})$ is the sum of the weights for each separation and $I(\mathbf{r})$, $I(\mathbf{r} + \mathbf{l})$ are the weights (i.e., intensities) of each pair of pixels. This form of the structure function obviously favours bright structures and reduces the contribution of fainter regions. This is one way to reduce the contribution of noise to the structure function. The figures show that once again, for the H α and [OIII] emission lines, there is little difference between these new structure functions (open symbols) and the number-of-points-weighted structure functions (solid symbols). However, ~~this time the [NII] structure functions are~~ is different, with the intensity weighting producing structure functions with shallower slopes (smaller power-law indices). For the shorter wavelength [SII] $\lambda 6716$ case, the intensity weighting makes little difference to the pdf-selected structure function (red circles) but does reduce the noise contribution to the full structure function (blue triangles) and leads to a similar power-law index to the pdf-selected cases over the fitted

range. For the longer wavelength [SII] $\lambda 6731$ case, the intensity weighting produces a shallower power law, even for the pdf-selected case (red circles). It is not possible to plot the intensity weighted structure function for the full set of pixels on the same scale because the contributions of regions of bad pixels both in the velocity centroid map and the intensity map dominate at all scales.

3.3 Analysis of power-law indices

We want to use the power-law indices from the velocity channel analysis and the second-order structure functions obtained from the spectroscopic observations to recover the three-dimensional velocity statistics of the ionized gas in the Orion Nebula. There are relationships between the power-law indices of the two-dimensional structure function of the emission-line velocity centroid map and the three-dimensional structure function of the velocity field. For projection from 3 to 2 dimensions we have $m_{2D} = m_{3D} + 1$, which is known as projection smoothing (von Hoerner 1951; Münch 1958; O'Dell & Castañeda 1987; Brunt & Mac Low 2004). If, however, the distribution of emitters is sheet-like, i.e., essentially two-dimensional, then $m_{2D} \approx m_{3D}$ (Castañeda & O'Dell 1987; Miville-Deschénes, Joncas, & Durand 1995). The three-dimensional structure function power-law index is related to the three-dimensional power spectrum spectral index (n) of the underlying velocity

For thin slice:

$$\sigma_t = 1 \text{ km/s} \Rightarrow \sigma_t^2 = 1 \text{ km}^2/\text{s}^2$$

BUT we also have the thermal and instrumental broadening — $\sigma_{\text{therm}}^2 \approx \frac{82 T_4}{A}$

$$[\text{OII}], [\text{NII}] : \sigma_{\text{therm}}^2 \approx 4 \text{ km}^2/\text{s}^2$$

$$[\text{SII}] : \sigma_{\text{therm}}^2 \approx 2 \text{ km}^2/\text{s}^2$$

Turbulence in the Ionized Gas of the Orion Nebula 9
Instrumental, FWHM $\approx 6 \text{ km/s} \Rightarrow \sigma \approx 2.5 \text{ km/s} \Rightarrow \sigma_{\text{ins}}^2 \approx 6 \text{ km}^2/\text{s}^2$

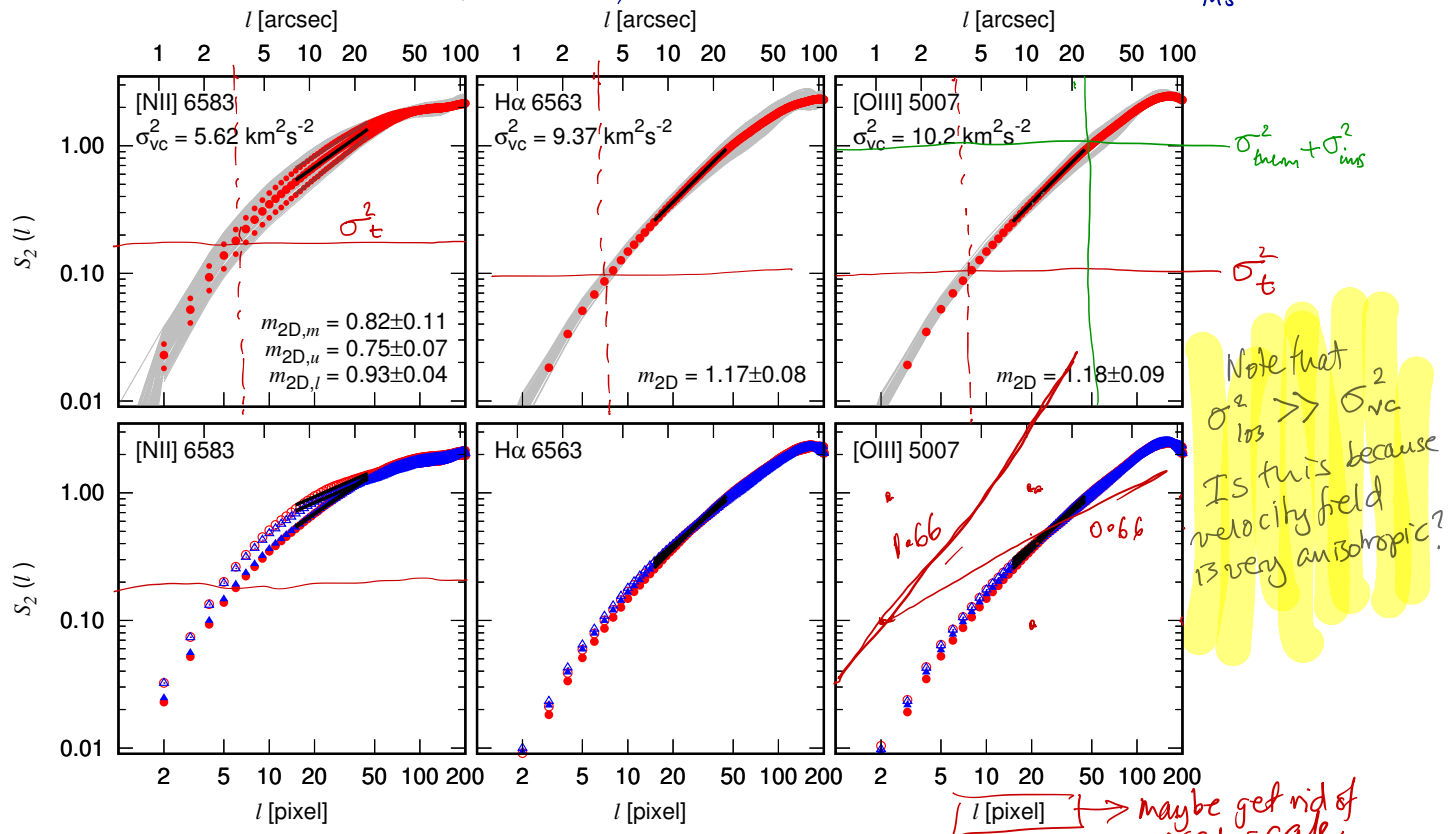


Figure 8. Second-order structure functions for the velocity centroid images of the [NII] $\lambda 6583$, H α and [OIII] $\lambda 5007$ emission lines considered in this work. Top panel (pdf-selected pixels): the structure functions of a random sample of 100 rectangles are shown with grey lines, the combined structure function is shown with red circles and the power-law fit to the combined structure function is shown with a thick black line. The power-law index of the fit and the standard deviation obtained by considering fits to the individual rectangle structure functions is indicated in each panel. The [NII] emission line shows a clear bimodal distribution and so fits to the upper and lower parts (60 and 40 rectangles, respectively) were also obtained separately (small red circles). Lower panel: number-of-points weighted structure functions (solid symbols) and intensity weighted structure functions (open symbols). Red circles are for the pdf-selected pixels from the velocity centroid maps whereas blue triangles are for the full velocity centroid map with no pixel selection. A pixel width is equivalent to $0.54''$ in the corresponding velocity centroid maps from which these structure functions were obtained.

field through $m_{3D} = -3 - n$, where $n = -\frac{11}{3}$ for homogeneous, incompressible turbulence.

The velocity channel analysis gives us the power-law indices of the average power spectra of thin and thick velocity slices. The thickest velocity slice corresponds to the velocity-integrated surface brightness and the power-law indices of the power spectra of the thick slices are predicted to be equal to the power indices of the 3D power spectra of the respective emissivities, i.e., $\gamma_T = n_E$ (Lazarian & Pogosyan 2000). However, if the emission has a sheet-like morphology, which is expected for the lower ionization lines like those of [SII] and [NII], Miville-Deschénes, Levrier, & Falgarone (2003) show that a shallower power-law index is appropriate, $\gamma_T = n_E + 1$. The critical value $n_E \sim -3$ divides ‘shallow’ power spectra from ‘shallow’ power spectra.

There are relations between the power-law index of the 3D velocity fluctuation power spectrum and the power-law indices of the VCA power spectra, depending on whether the power spectrum of the emissivity fluctuations is ‘steep’ or ‘shallow’ (Lazarian & Pogosyan 2000). In the steep case, the power-law index of the average power spectrum of the thin isovelocity channels is given by

$$\gamma_t = -3 + \frac{1}{2} m_{3D},$$

Regime III is always steep.
BUT not clear that any slices are “thin” at Regime II

where $m_{3D} = -3 - n$ is defined above. For the ‘shallow’ regime, the relation is with the difference in the power-law indices of the average power-spectra of the thin and thick velocity slices:

$$\gamma_t - \gamma_T = \frac{1}{2} m_{3D}.$$

Regime II is always shallow.
except for [SII], which is borderline

3.3.1 VCA: wavenumbers in the range

$$0.044k < 0.124 \text{ arcsec}^{-1}$$

This is Regime II

We consider each emission line in turn, beginning with the SII lines, which represent the lowest ionization state of our data. For the low wavenumber range, corresponding to spatial scales > 7 arcsec, the power-law indices of the thick slice power spectra are $\gamma_T = -3.06$ and $\gamma_T = -3.03$ for the [SII] $\lambda 6716$ and [SII] $\lambda 6731$ lines, respectively. This is the critical value separating ‘steep’ from ‘shallow’ power spectra. Taking the difference in power-law indices between the thin and thick slice power spectra we obtain $\gamma_t - \gamma_T = 0.34 \pm 0.18$ for both [SII] lines and relate this to the 3D second-order structure function using Equation 6. This gives

SEE FIG 8

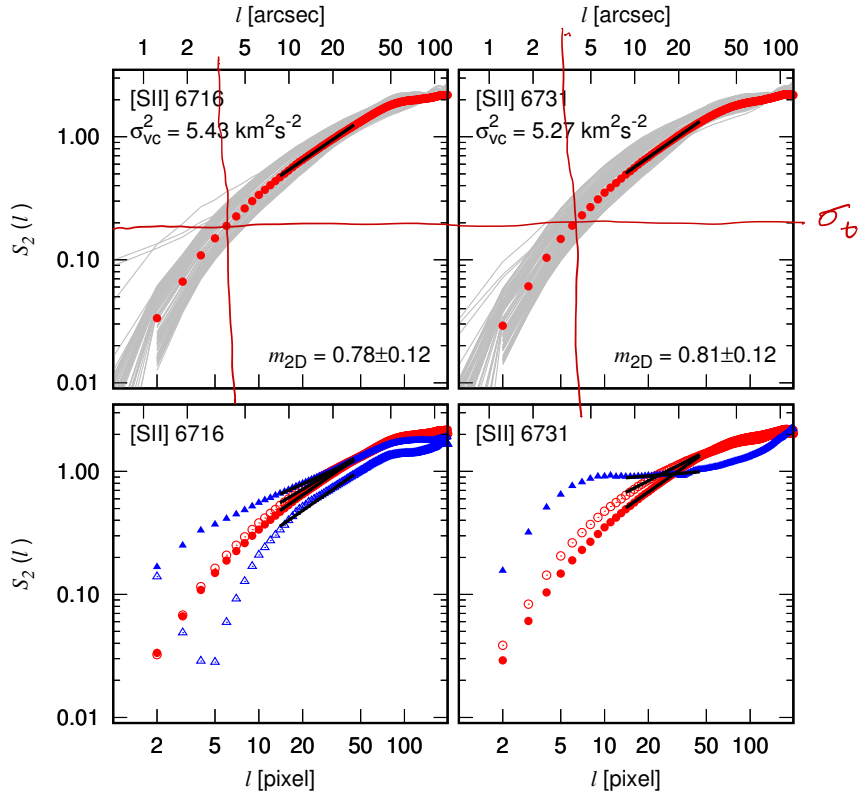


Figure 9. Same as Fig. 8 but for the [SII] $\lambda 6716$ and [SII] $\lambda 6731$ emission lines. A pixel width is equivalent to $0.62''$ in the corresponding velocity centroid maps from which these structure functions were obtained.

$m_{3D} = 0.68 \pm 0.36$, which results in $n = -3.68 \pm 0.36$, where n is the power-law index of the 3D power spectrum of the velocity fluctuations. If we treat the power spectra as belonging to the ‘steep’ regime, we apply Equation 5 to obtain $m_{3D} = 0.56 \pm 0.24$ and $m_{3D} = 0.62 \pm 0.22$ for the short and long wavelength [SII] lines, respectively. The corresponding power-law indices of the 3D velocity fluctuations are then $n = -3.56 \pm 0.24$ and $n = -3.62 \pm 0.22$, respectively. Note that whichever regime is assumed, the values of n are consistent with the Kolmogorov value of $n = -3.67$. The [SII] lines are least affected by thermal broadening and, moreover, the 20 spectra used to calculate the power spectra have the highest velocity resolution of all our observational data.

Moving to higher ionization lines, the calculated ‘thick’ and ‘thin’ slice power-law indices of the [NII] $\lambda 6583$ spectra fall into the ‘shallow’ regime. Following the same analysis as above, we recover $n = -3.56 \pm 0.24$, which is again close to the Kolmogorov value. For the H α power spectra, there is little difference between the thin and thick power-law indices since thermal broadening is important for this line (see, e.g., Paper I). It is therefore not possible to recover a meaningful value of n . Finally, the [OIII] $\lambda 5007$ power spectra again fall into the ‘shallow’ regime and we obtain $n = -3.58 \pm 0.26$.

It is gratifying that the [NII], [OIII] and [SII] power spectra power-law indices are consistent with each other and with the Kolmogorov value, within the errors.

3.3.2 VCA: wavenumbers in the range $0.213 > k > 0.124 \text{ arcsec}^{-1}$

For the high wavenumber range (corresponding to small spatial scales), only the [SII] $\lambda 6716$ and [SII] $\lambda 6731$ power spectra have ‘thick’ slice power-law indices steeper than their ‘thin’ slice power-law indices. The [NII], H α and [OIII] have curiously opposite behaviour and their power-law indices cannot be accommodated by the theory. For the [SII] power spectra, the value of γ_T falls into the ‘steep’ regime. However, for both [SII] lines, the value of γ_T is less than -3 and so this would lead to negative values for m_{3D} on applying Equation 5. We postulate that this wavenumber range corresponds to the energy dissipation range and that power is lost rapidly from the system for lengthscales $l < 8 \text{ arcsec}$.

Possible that slices are no longer thin in this regime if $\Delta v @ 5'' < 4 \text{ km/s}$

3.3.3 Structure function power indices

We fit the structure functions over the pixel separation range $15 < l < 45$, which corresponds to the wavenumber range suggested by the VCA analysis. The structure function graphs themselves do not strongly suggest that any particular range is preferable, although in the range $l < 8$ the structure function falls off very steeply because this corresponds to a loss of resolution due to seeing?. At the largest separations, the structure function power-law index flattens off, i.e. $m_{2D} \sim 0$ for $l > 100$. Over the separation range we fit, we find $0.75 < m_{2D} < 1.2$ for all lines, with H α and [OIII] having the steepest power-law indices.

The 2D power-law indices for the [NII] $\lambda 6853$,

Kolmogorov : $n = -3.66$

$m_{3D} = 0.66$

$m_{2D} = 0.66 \rightarrow 1.66$
sheet volume

Here make comparison with
simulation results. And with
what the VCA results predict for SF slopes.

[SII] $\lambda 6716$ and [SII] $\lambda 6731$ lines are all $m_{2D} < 1$, which suggests that the distribution of emitting gas is sheet-like. In this case, the 2D and 3D power-law indices should be comparable, i.e. $m_{2D} \sim m_{3D}$. Hence, for [NII] we recover $m_{3D} = 0.75$ and $m_{2D} = 0.93$ for the two distributions that are apparent in Figure 8, while for the [SII] $\lambda 6716$ we find $m_{3D} = 0.80$ and for [SII] $\lambda 6731$ we find $m_{3D} = 0.82$. Using the relation between the structure function power-law index and the power-law index of the 3D velocity fluctuations, $m_{3D} = -3 - n$, we would have $n > 3.67$ for all of these cases, which is not consistent with the results of the Velocity Channel Analysis, nor with the Kolmogorov value.

Turning to the H α and [OIII] structure function power-law indices, in both cases $m_{2D} > 1$, suggesting that projection smoothing plays a role. Accordingly, we use the relation $m_{2D} = 1 + m_{3D}$, which gives us $m_{3D} = 0.17$ for the H α structure function and $m_{3D} = 0.18$ for the [OIII] case. Thus we recover $n = -3.17$ and $n = -3.18$ for the respective power-law indices of the underlying 3D velocity fluctuations, which again are neither consistent with the Velocity Channel Analysis, nor with the Kolmogorov value.

In conclusion, the 2D structure function power-law indices give us confusing information. Evidently, the distribution of the emitting gas for all lines is intermediate between the ‘sheet-like’ and volume distributed cases (which implies projection smoothing should be taken into account). The power-law indices are not consistent with the results found from the Velocity Channel Analysis nor with the theoretical expectations. The reasons for this could include not taking into account the form of the line profile, for example, a double-peaked line profile would have a velocity centroid value between the velocities corresponding to the intensity peaks.

What else can we learn from the structure functions: scale corresponding to turnover tells us about...?

4 DISCUSSION

4.1 Comparison with other observations

Castañeda and O’Dell. Miville-Dechenes.

Castañeda (1988) calculate structure functions for the [OIII] emission line. Their data consist of slits at different position angles in the region around Theta 1C. The velocity variation among slits passing through the same pixel is used to evaluate the errors for the different components of the emission lines. Systematic velocity variations (e.g., large scale velocity gradient due to the champagne flow) are removed and the spectral lines are separated into 3 components before calculating the structure function for each component. They find a relatively steep power law ($m_{2D} \sim 0.86$) for the main A component for scales $\Lambda < 15$ arcsec. The structure function then flattens off between 15 and 35 arcsec before steepening again. Instead of a break in the power law our results show a gradual change, with the power-law index becoming shallower at larger separations. For the range of separations that we fit, $8 < l < 24$ arcsec, we find an even steeper power law ($m_{2D} = 1.18$ than that reported by Castañeda (1988).

Castañeda (1988). use a limited number of radial slits distributed more-or-less radially around Theta 1C, which

means that the central regions are overrepresented compared to more distant regions. The values of $B(\Lambda)$ (i.e., the normalization of the structure function) given by (Castañeda 1988) for Component A at a separation scale of 20 arcsec ($B(\Lambda = 20) \sim 9.3 \text{ km}^2 \text{s}^{-2}$) are similar to our values of $\sigma_{\text{vc}}^2 \sim 10.2 \text{ km}^2 \text{s}^{-2}$ for [OIII].

A similar study using slit spectra was performed by Wen & O’Dell (1993) for the [SIII] $\lambda 6312 \text{ \AA}$ emission line. The data were analysed in a similar way to Castañeda (1988): large-scale velocity gradients were removed and different velocity components were identified. The structure function was calculated for the (strongest) A component only. Wen & O’Dell (1993) find a structure function for the [SIII] principal component system quite similar to the result of Castañeda (1988) for [OIII]. That is, a steep power-law index, $m_{2D} \sim 0.92$, for separation scales below 25 ”, which becomes almost flat at larger separations. They remark that the S⁺⁺ and O⁺⁺ ions share a large common zone. Again, the region covered by the slit observations of Wen & O’Dell (1993) is concentrated in the central region around Theta 1C.

Neither the Castañeda (1988) results, nor those of Wen & O’Dell (1993) agree with the values expected for Kolmogorov theory, i.e. $m_{2D} = 5/3$, nor even with the theory of von Hoerner (1951), which predicts $m_{2D} = 2/3$ for a two-dimensional (i.e., sheet-like) distribution of emitters. On the other hand, within the errors, our power-law indices are consistent with these two previous studies for separation scales below 25 arcsec. Our data are more complete at larger separations in that our velocity centroid maps cover a rectangular region measuring 200x260 arcsec of the Orion nebula around Theta 1C and are not concentrated in a central region. However, our intensity weighted structure functions are very similar to the number-of-points weighted structure functions (see Fig. 8), particularly for [OIII], and so these fainter outer regions do not modify the shape of the structure function or steepness of the power-law. On the other hand, we do not separate our spectra into individual components, which will produce some differences between our velocity centroid values and the central velocities of the [OIII] system component A reported by Castañeda (1988).

A more recent analysis of the turbulent velocity field of the central Orion Nebula is that of Mc Leod et al. (2016), which is based on MUSE integral field observations. For the [OIII] $\lambda 5007$ emission line they find a very shallow structure function, with a power-law index of only $m_{2D} = 0.29$ over the range of separation scales $0.015 < l < 0.148$ pc, which corresponds to angular separations $8 < l < 72$ arcsec, assuming a distance of 420 pc to the Orion Nebula (Schlafly et al. 2014). Moreover, they find no break in the structure function and the turnover occurs for angular separations $l > 80$ arcsec. The area covered by their observations measures 6x5 arcmin and includes large regions of low signal-to-noise in the emission lines. Mc Leod et al. (2016) assess the contribution of noise to their structure function and their reported value of the power-law index is for masked data, whereby pixels with intensity below a threshold value are discarded. The unmasked data produces an even shallower structure function power-law index. Unfortunately, Mc Leod et al. (2016) normalize their structure functions to the peak value and do not report the normalization value. The masked [OIII] data includes large areas of very low velocity

I wouldn't
spend so many
words on
the McLeod
stuff.
Alternatively,
we could
re-do it -
from new
data....

Things to add — why do all emissivity power spectra show change in slope @ 8 arcsec?
The fact that our thin slices show Kolmogorov slopes only in range of 8-30" doesn't mean that this is necessarily all of the metal range — it could extend to smaller scales, but our slices are no longer thin here.

(with respect to the mean), which are outside the region covered by our study (this could be confirmed if the normalization value were given for the structure function). These pixels will have a major contribution to the (number-of-points weighted) structure function and result in a shallow power-law index. If the structure function were intensity weighted, the structure function would probably be steeper. The H α structure function shown by Mc Leod et al. (2016) has a power-law index of $m_{2D} = 0.46$ for the separation range $20 < l < 98$ arcsec, much steeper than the value they find for [OIII] but still much lower than that found in our study ($m_{2D} = 1.17$, the same as we find for [OIII]). Again, the masked region contains large numbers of pixels with low velocity (relative to the mean), which will flatten the structure function. These pixels are predominantly found in regions of low surface brightness.

As a comparison, (Miville-Deschénes, Joncas, & Durand 1995) obtained a power-law index of $m_{2D} \sim 0.8$ for the HII region Sharpless 170 from analysis of more than 12,000 H α radial velocities measured across the nebula with a Fabry-Perot instrument. Sh 170 is a small, faint HII region with a diameter of 20 arcmin at an assumed distance of 2.3 kpc, i.e., the spatial extent of the nebula is about 13.4 pc. Prior to calculating the structure function they removed the large-scale, north-south velocity gradient of $1.4 \text{ km s}^{-1} \text{ pc}^{-1}$ from the data. The inertial range identified for this object is $0.03 < l < 0.07$ pc, which is very narrow compared to the diameter of the HII region (note that after data reduction, the spatial resolution of the data is 1 arcsec, which corresponds to 0.011 pc at the distance of the object). The variance of the velocity centroids is $\sigma_{vc}^2 \sim 75 \text{ km}^2 \text{s}^{-2}$. At larger scales the structure function is flat. *Far larger than we see in Orion*

In summary, the second order structure function is a very unreliable statistic for analyzing the turbulent velocity field of the ionized gas. The slope of the structure function depends very much on the region covered by the study, how the noise is treated and how regions of low surface brightness are taken into account. Also, it makes some difference whether the lines are split into individual components and if large-scale velocity gradients are removed prior to statistical analysis. In any case, none of the reported observational results support the Kolmogorov theory ($m_{2D} = 5/3$, assuming projection smoothing) or the modification proposed by von Hoerner (1951) for a sheet-like distribution of emitters ($m_{2D} = 2/3$).

Velocity Channel Analysis is optimally applied to spatially resolved PPV data from optically thin emission lines and can be used when the turbulence is supersonic, unlike the velocity centroid statistics, which are best employed when the turbulence is subsonic or at most mildly supersonic (Lazarian 2004). It has been applied to the HI gas in the Galaxy (Lazarian & Pogosyan 2000) and in the SMC (Stanimirović & Lazarian 2001). There are no previous VCA studies of the ionized gas in the Orion Nebula (or any other ionized gas VCA studies of which we are aware) but the conditions apply: our longslit spectra are spatially resolved and the emission lines are optically thin. However, we do not have PPV cubes — our data are in the form of longslit (PV) spectra and so we calculate the 1D power spectra. The finite length of our slits leads to ringing due to edge effects in the calculated power spectrum, which would not be present if

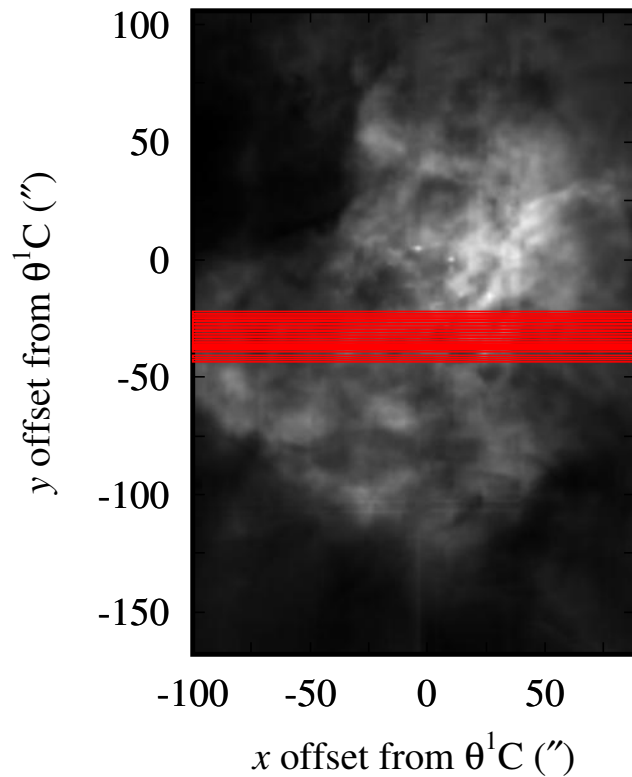


Figure 10. Positions of the horizontal slits superimposed on the [OIII] surface brightness image.

we were calculating the 2D power spectra of velocity slices of PPV cubes.

Supplementary to the data obtained by García-Díaz et al. (2008) we also have [OIII] $\lambda 5007$ observations from 18 slit positions perpendicular to the main data set, which we have not used in our analysis up to now; the slit positions and orientations are indicated in Figure 10 (O'Dell et al. 2015). Figure 11 shows the results of a velocity channel analysis of these 18 slits, using the same procedure as described in Sections 2.1 and 3.1

Velocity centroid statistics only good if density effects not confused with velocity effects - ie incompressible (or subsonic).

sumlich
this
go in
the
results
section.

4.2 Comparison with simulation results

Power-law indices. Physical processes not included in simulations.

and this as well
should be in the results part.

5 SUMMARY AND CONCLUSIONS

REFERENCES

- Arthur S. J., Henney W. J., Meléndez G., de Colle F., Vázquez-Semadeni E., 2011, MNRAS, 414, 1747
- Brunt C. M., Heyer M. H., 2002, ApJ, 566, 276
- Brunt C. M., Heyer M. H., Vázquez-Semadeni E., Richardson B., 2003, ApJ, 595, 824
- Brunt C. M., Mac Low M.-M., 2004, ApJ, 604, 196
- Castañeda H. O., 1988, ApJS, 67, 93

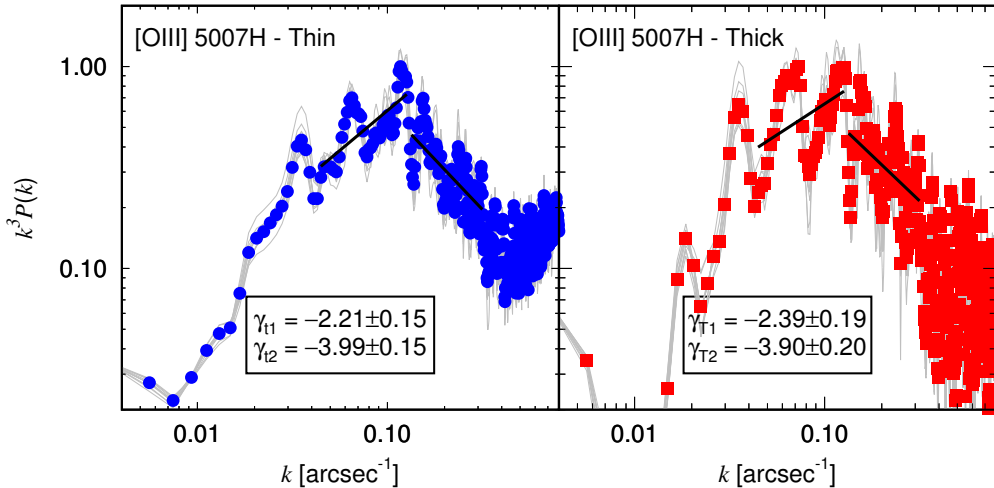


Figure 11. Same as Fig. 5 but for the [OIII] 5007 horizontal slits.

- Castañeda H. O., O'Dell C. R., 1987, ApJ, 315, L55
 Chandrasekhar S., 1949, ApJ, 110, 329
 Esquivel A., Lazarian A., 2005, ApJ, 631, 320
 Esquivel A., Lazarian A., Horibe S., Cho J., Ossenkopf V., Stutzki J., 2007, MNRAS, 381, 1733
 Esquivel A., Lazarian A., Pogosyan D., Cho J., 2003, MNRAS, 342, 325
 García-Díaz M. T., Henney W. J., 2007, AJ, 133, 952
 García-Díaz M. T., Henney W. J., López J. A., Doi T., 2008, RMxAA, 44, 181
 Henney W. J., Arthur S. J., de Colle F., Mellemma G., 2009, MNRAS, 398, 157
 Kolmogorov A., 1941, DoSSR, 30, 301
 Kritsuk A. G., Norman M. L., Padoan P., Wagner R., 2007, ApJ, 665, 416
 Lagrois D., Joncas G., 2011, MNRAS, 413, 721
 Lagrois D., Joncas G., Drissen L., Arsenault R., 2011, MNRAS, 413, 705
 Lazarian A., 2004, ASSL, 319, 601
 Lazarian A., Pogosyan D., 2000, ApJ, 537, 720
 Mc Leod A. F., Weilbacher P. M., Ginsburg A., Dale J. E., Ramsay S., Testi L., 2016, MNRAS, 455, 4057
 Medina S.-N. X., Arthur S. J., Henney W. J., Mellemma G., Gazol A., 2014, MNRAS, 445, 1797 (Paper I)
 Medina Tanco G. A., Sabalisck N., Jatenco-Pereira V., Opher R., 1997, ApJ, 487, 163
 Mellemma G., Arthur S. J., Henney W. J., Iliev I. T., Shapiro P. R., 2006, ApJ, 647, 397
 Mellemma G., Iliev I. T., Alvarez M. A., Shapiro P. R., 2006, NewA, 11, 374
 Miville-Deschénes M.-A., Joncas G., Durand D., 1995, ApJ, 454, 316
 Miville-Deschénes M.-A., Levrier F., Falgarone E., 2003, ApJ, 593, 831
 Münch G., 1958, RvMP, 30, 1035
 O'Dell C. R., 1986, ApJ, 304, 767
 O'Dell C. R., Castañeda H. O., 1987, ApJ, 317, 686
 O'Dell C. R., Ferland G. J., Henney W. J., Peimbert M., García-Díaz M. T., Rubin R. H., 2015, AJ, 150, 108
 O'Dell C. R., Henney W. J., 2008, AJ, 136, 1566
 O'Dell C. R., Townsley L. K., 1988, A&A, 198, 283
 O'Dell C. R., Townsley L. K., Castañeda H. O., 1987, ApJ, 317, 676
 O'Dell C. R., Wen Z., 1992, ApJ, 387, 229
 Roy J.-R., Joncas G., 1985, ApJ, 288, 142
 Schlafly E. F., et al., 2014, ApJ, 786, 29
 Stanimirović S., Lazarian A., 2001, ApJ, 551, L53
 Vázquez-Semadeni E., Kim J., Ballesteros-Paredes J., 2005, ApJ, 630, L49
 von Hoerner S., 1951, ZA, 30, 17
 Wen Z., O'Dell C. R., 1993, ApJ, 409, 262